The Planetary Science Journal, 4:14 (12pp), 2023 January https://doi.org/10.3847/PSJ/acaf6a

The Solar Wind Interaction with (1) Ceres: The Role of Interior Conductivity

A. R. Poppe[1], and S. Fatemi[2]
[1] Space Sciences Laboratory, University of California at Berkeley, Berkeley, CA 94720, USA; poppe@berkeley.edu
[2] Department of Physics, Umeå University, Umeå, Sweden
Received 2022 October 11; revised 2022 December 27; accepted 2022 December 30; published 2023 January 25

Abstract

As a potential "ocean world," (1) Ceres' interior may possess relatively high electrical conductivities on the order of 10^{-4}–10^{0} S m^{-1}, suggesting that the solar wind interaction with Ceres may differ from other highly resistive objects such as the Moon. Here, we use a hybrid plasma model to quantify the solar wind interaction with Ceres over a range of scenarios for Ceres' internal conductivity structure and the upstream solar wind and interplanetary magnetic field (IMF) conditions. Internal models for Ceres include one-, two-, and three-layer conductivity structures that variously include a crust, mantle, and/or subsurface ocean, while modeled solar wind conditions include a nominal case, a high IMF case, and an "extreme" space weather case. To first order, Ceres' interaction with the solar wind is governed by the draping and enhancement of the IMF over its interior, whether from a moderate-conductivity mantle or a high-conductivity ocean. In turn, IMF draping induces compressional wings in the solar wind density and deceleration in the solar wind speed outside of Ceres. Together, all three effects are readily observable by a hypothetical orbital or landed mission with standard plasma and magnetic field instrumentation. Finally, we also consider the possible effects of unipolar induction within Ceres, which has been previously suggested as a mechanism for conducting bodies in the solar wind. Our model results show that the efficacy of unipolar induction is highly suppressed by the slow magnetic field-line diffusion through Ceres' interior and, thus, is not a significant contributor to Ceres' overall interaction with the solar wind.

Unified Astronomy Thesaurus concepts: Ceres (219); Planetary interior (1248); Solar wind (1534); Interplanetary magnetic fields (824)

1. Introduction

With a mean radius of $R_C = 470$ km, (1) Ceres is the largest asteroid in the main asteroid belt and the innermost dwarf planet. Ceres has reached a state near hydrostatic equilibrium and has undergone partial differentiation in its interior (Park et al. 2016; King et al. 2018), with typical models for Ceres' structure assuming an outer, ice- and volatile-rich crust and an inner, more silicate-rich "mantle" (e.g., Castillo-Rogez 2011; Ermakov et al. 2017). Observations by the Dawn spacecraft (Russell et al. 2007) of freshly emplaced salts on the surface of Ceres have suggested the continued presence of liquid water within Ceres (e.g., De Sanctis et al. 2020; Bramble & Hand 2022); however, it is not immediately clear if these signatures are indicative of an extant global ocean today or of residual internal brines that occasionally reach the surface. Based on these works, Grimm et al. (2021) postulated two- and three-layer electrical conductivity models for the interior structure of Ceres in a study of time-dependent electromagnetic sounding of Ceres' interior. In the two-layer model, a 35 km thick crust with conductivity $\sigma_c = 10^{-4}$ S m^{-1} overlays a phyllosilicate mantle with conductivity $\sigma_m = 10^{-2}$ S m^{-1}. The three-layer model possesses a 35 km thick crust with $\sigma_c = 10^{-4}$ S m^{-1}, a 65 km thick, highly conducting "ocean" with $\sigma_o = 10^{0}$ S m^{-1}, and a phyllosilicate mantle with $\sigma_m = 10^{-2}$ S m^{-1}. In either case, the relatively high conductivity of Ceres' internal layers suggests that its interaction with the solar wind may be in a distinctly different class than other airless bodies in the solar system such as the Moon, which possesses much more resistive outer layers (e.g., Olhoeft et al. 1974; Khan et al. 2006; Grimm & Delory 2012).

The physics of solar wind interactions with conductive planetary obstacles has primarily focused on induced magnetospheres that arise as a result of ionized planetary atmospheres, such as occurs at Venus, Mars, Titan, and various comets (e.g., Luhmann et al. 2004; Coates & Jones 2009; Bertucci et al. 2011; Glassmeier 2017). Here, the production of newly born, often heavy planetary (or cometary) ions via photo-, electron-impact, or charge-exchange ionization results in mass loading and overall momentum and energy extraction from the solar wind or planetary magnetospheric flows. In turn, ambient flowing magnetic fields and plasma pile up and compress in front of the obstacle, generating a so-called "induced magnetosphere." In contrast, the study of induced magnetospheres at airless bodies with relatively highly conducting interiors has been less explored. Oran et al. (2018) used a magnetohydrodynamic (MHD) approach to model the interaction of a Ceres-sized object with radially varying conductivity between 10^{-3} and 10^{-5} S m^{-1} with the early solar wind to investigate the possibility of chondrite magnetization via pile-up and enhancement of solar wind fields. The use of an MHD model—as opposed to the hybrid model used here—was justified in their case due to significantly different upstream solar wind conditions during the early solar system era. Their results showed interplanetary magnetic field (IMF) draping and the formation of an induced magnetosphere capable of enhancing the local field strength by more than a factor of 3. At Mercury, Jia et al. (2015) investigated the coupled interaction of Mercury's intrinsic magnetosphere and induced fields originating from Mercury's highly conductive core. They found that abrupt changes in the solar wind conditions can trigger induced fields capable of strongly altering the overall magnetospheric

structure and the patterns in which the solar wind can precipitate to Mercury's surface. On a smaller scale, Fatemi & Poppe (2018) presented hybrid simulation results of the asteroid (16) Psyche under the assumption of a highly conductive composition ($\sigma \sim 10^1$ S m^{-1}) without a global, permanent magnetic dipole, showing strong field-line draping and downstream disturbances in the solar wind.

At Ceres, the nature of its interaction with the modern-day solar wind with the inclusion of conductive interior layers (e.g., Grimm et al. 2021) remains almost completely unstudied. Both Kallio et al. (2008) and Lindkvist et al. (2017) have modeled the solar wind interaction with Ceres (the latter investigation with ionization of a water-vapor exosphere); however, both investigations modeled Ceres as a fully resistive object. A separate study by Jia et al. (2017) explored a number of different scenarios for the solar wind interaction with Ceres in an effort to understand the possible formation of an upstream bow shock and fast-Fermi acceleration of electrons as observed by the Dawn spacecraft (Russell et al. 2017; Villarreal et al. 2017). While most of the scenarios studied in Jia et al. (2017) centered around the effects that a global water-vapor exosphere or more localized plume had on the solar wind interaction, one of their cases modeled a uniform, perfectly conducting object in place of Ceres to investigate the possibility of induced magnetization. Under such conditions, Jia et al. (2017) reported the formation of a shock upstream of Ceres, albeit one weaker than that formed by exospheric outgassing. In the end, Jia et al. (2017) discarded the possibility that a highly conducting Ceres could explain the relatively long-lived bursts of high-energy electrons inferred by Dawn and did not model any more complex or realistic conditions for the interior conductivity structure of Ceres.

We also examine an additional, somewhat more exotic possibility that the solar wind interaction with Ceres may be affected by a process known as "unipolar induction," in which direct currents are induced within a conductive planetary interior by the passage of the motional electric field of the solar wind, $\boldsymbol{E}_c = -\boldsymbol{v} \times \boldsymbol{B}_{\rm sw}$ (e.g., Sonett & Colburn 1967, 1968). In turn, these currents generate a toroidal magnetic field within the body that pushes back on the solar wind dynamic pressure and, if strong enough, may trigger the formation of an upstream bow shock. Unipolar induction has previously been considered in the context of the solar wind interactions with the Moon and asteroids (e.g., Sonett & Colburn 1967, 1968; Schwartz et al. 1969; Sonett et al. 1970; Dyal & Parkin 1971; Herbert 1989; Shimazu & Terasawa 1995; Menzel & Roberge 2013), planetary satellite interactions with their parent-planet magnetospheres (e.g., Goldreich & Lynden-Bell 1969; Herbert & Lichtenstein 1980; Colburn & Reynolds 1986; Saur 2004; Hand et al. 2011), and stellar magnetosphere interactions with close-in exoplanets (e.g., Li et al. 1998; Laine & Lin 2012; Walters et al. 2021). Unipolar induction is distinct from the induced fields generated by time-dependent changes in upstream electromagnetic fields, which have previously been used or proposed for electromagnetic sounding of planetary interiors (e.g., Khan et al. 2006; Grimm & Delory 2012; Jia et al. 2015; Haviland et al. 2019; Mittelholz et al. 2021). In contrast, the generation of unipolar-induced magnetospheres in planetary objects and their interaction with ambient plasma has not, to our knowledge, been previously studied with self-consistent numerical plasma models.

In this study, we use a three-dimensional hybrid plasma model to investigate the solar wind interaction with Ceres. In particular, we investigate various scenarios for the internal structure of Ceres, including a single-layer, fully resistive interior; a series of one-, two-, and three-layer interiors with moderate to high conductivities; and a single-layer conductive interior with the inclusion of unipolar currents. In Section 2, we describe the hybrid plasma model, detailing in particular the newly implemented routine for modeling the unipolar current and magnetic field contributions. In Section 3, we present and describe the model results for all three modeled conditions at Ceres. Finally, we discuss the implications of our results and conclude in Section 4.

2. Model Description

2.1. Baseline Model

To self-consistently model the solar wind interaction with Ceres, we used the Amitis hybrid plasma model (Fatemi et al. 2017). Amitis is a three-dimensional, GPU-based, quasi-neutral hybrid plasma model that has been extensively used to simulate space plasma interactions with planetary bodies (e.g., Fatemi & Poppe 2018; Fatemi et al. 2018, 2020, 2022; Garrick-Bethell et al. 2019; Haviland et al. 2019; Poppe 2019; Rasca et al. 2021; Shi et al. 2022). The model uses a standard, body-centered Cartesian coordinate system, where the $+x$ axis points from the center of the body to the Sun, the $+z$ axis points toward ecliptic north, and the $+y$ axis completes the right-handed set. We modeled Ceres as a spherical object with 475 km radius (Ceres' ellipsoidal shape is $482 \times 482 \times 446$ km; Park et al. 2019) using a Cartesian mesh with cubic grid cells of $20 \times 20 \times 20$ km^3. For our study, we did not include the presence of ionized material from a neutral exosphere at Ceres (see Küppers et al. 2014; Roth et al. 2016; Jia et al. 2017; Lindkvist et al. 2017). All simulations were run past the establishment of steady-state plasma conditions as determined by the time evolution of fields and densities in the vicinity of Ceres; however, we note that the interior magnetic diffusion timescales in cases with relatively high interior conductivity (e.g., $\sigma \geqslant \sim 10^{-3}$) are computationally prohibitive to model all the way to full interior steady state. This is a known limitation of current-day computational resources (e.g., see also Oran et al. 2018) and should be kept in mind through the following study. At the surface of Ceres, all solar wind ions are absorbed and removed from the simulation, while the magnetic field is allowed to diffuse through the body via an application of the magnetic diffusion equation. A full description of the boundary conditions and the use of the magnetic diffusion equation in modeling the interior of Ceres can be found in Fatemi et al. (2017).

We defined a baseline set of solar wind and IMF conditions using median solar wind parameters in the main asteroid belt as compiled by Collinson et al. (2022), which are relevant for objects roughly at the orbital distance of Ceres (2.55−2.98 au): solar wind density, $n_{\rm sw} = 0.75$ cm^{-3}; solar wind velocity, $v_{\rm sw} = 400$ km s^{-1}; ion temperature, $T_i = 4$ eV; electron temperature, $T_e = 8$ eV; and IMF, $\boldsymbol{B}_{\rm sw} = [-0.50,\ 1.9,\ 0.0]$ nT ($|B| = 1.96$ nT). Under these conditions, the convective electric field is $\boldsymbol{E}_{\rm sw} = -\boldsymbol{v}_{\rm sw} \times \boldsymbol{B}_{\rm sw} = [0.0,\ 0.0,\ +0.76]$ mV m^{-1} and the solar wind dynamic pressure is $P_{\rm sw} = 0.20$ nPa. Furthermore, the electron and ion inertial lengths are approximately 6 and 260 km, respectively, and the thermal ion gyroradius is

approximately 150 km; thus, modeling the solar wind interaction with Ceres (radius of 475 km) is firmly within the hybrid regime (e.g., Figure 3 of Fatemi et al. 2017). Note that these conditions describe the standard, reference case for our simulations; however, variations from these solar wind/IMF conditions are explored, as described below in Section 2.3.

2.2. Unipolar Current Model

In addition to the standard hybrid field-solving approach (e.g., Ledvina et al. 2008; Fatemi et al. 2017), we added a new subroutine within Amitis to include the formation and self-consistent interaction of unipolar fields within a conducting body (e.g., Sonett & Colburn 1968). The unipolar current within the body, assumed to be spatially uniform for simplicity, is computed from

$$\begin{aligned} \boldsymbol{J}_{\rm uni} &= \min(\sigma) \cdot \bar{\boldsymbol{E}}_c \\ &= \min(\sigma) \cdot (-\bar{\boldsymbol{v}}_c \times \bar{\boldsymbol{B}}), \end{aligned} \quad (1)$$

where $\min(\sigma)$ is the minimum conductivity of the object (under the assumption that the minimum conductivity occurs in the outermost layer), $\bar{\boldsymbol{E}}_c$ is the convection electric field within the body, $\bar{\boldsymbol{B}}$ is the magnetic field within the body, and $\bar{\boldsymbol{v}}_c$ is the convection speed of field lines through the body. The magnetic field, $\bar{\boldsymbol{B}}$, is computed from the average of the IMF/plasma interaction fields within the body. The convection speed of the field lines through the body is taken as the lesser of either (i) the local solar wind convection velocity as determined from the model macroparticles along the upstream hemisphere ($x > 0$) of the body, or (ii) the diffusion speed of magnetic field lines through the body. The solar wind convection velocity is computed along the upstream hemisphere of the body in order to self-consistently account for any deceleration and/or deflection that the solar wind may experience as it interacts with Ceres. The magnetic diffusion speed is calculated by assuming that in the presence of a conducting body, IMF lines will diffuse through the interior over a finite timescale, given approximately by $\tau_d = \mu_0 \sigma L^2/2$, where μ_0 is the permeability of free space, σ is the interior conductivity, and L is the object scale size (e.g., Equation (38) and surrounding discussion of Sonett & Colburn 1968). Equivalently, one can express this as an upper limit on the "diffusion speed" of a field line through the body as $v_d \approx L/\tau_d = 2/(\mu_0 \sigma L)$. Taking the lesser of these two velocities (solar wind ion speed versus magnetic diffusion speed) is necessary because one or the other will always be the limiting factor in convecting field lines through the body of Ceres and thus powering the unipolar inductor. If the diffusion speed is slower than the solar wind speed, then the IMF will pile up on the upstream hemisphere of Ceres and the local field-line convection speed through Ceres (which powers the unipolar conductor) will be limited by the diffusion speed. In contrast, if the solar wind speed is slower than the diffusion velocity, then the only limiting factor to the unipolar generator is the convection of field lines past the body. We note an important limitation with respect to the convection speed of IMF lines through Ceres in the unipolar current mechanism modeled here. Notably, for a 475 km thick object with a uniform conductivity of $\sigma_m = 10^{-4}$, the diffusion speed is only $\sim$16 km s^{-1}, far less than the typical solar wind velocity. Thus, to first order, the unipolar current is likely to be limited in its effects at Ceres; however, we nevertheless explore this scenario in our simulations as described below.

Once the unipolar current is computed, the Biot–Savart law is used to compute the unipolar magnetic field, $\boldsymbol{B}_{\rm uni}$, throughout the entire model domain (both within and outside of the body). Finally, $\boldsymbol{B}_{\rm uni}$ is then added to the magnetic fields determined from plasma currents (i.e., those calculated from Faraday's law, $\partial B/\partial t = -\nabla \times E$) at each timestep. For clarification, we note that the particular challenge in implementing the unipolar current within the hybrid model is that within the body of Ceres the only charge carriers available to produce a current are electrons, since ions are bound in the solid material. However, a hybrid model—by definition—does not have particle electrons and cannot naturally represent an electron-driven unipolar current within the body. In contrast, a particle-in-cell model should theoretically be able to directly implement a unipolar current; however, this is beyond the scope of the current study. Thus, given this limitation, we are left with the approach of analytically calculating the unipolar current (Equation (1), above) and adding in the resulting unipolar magnetic field to the model.

2.3. Description of Runs

With the Amitis hybrid model as described above, we ran 10 cases exploring the effects of varying solar wind/IMF conditions, the internal conductivity profile of Ceres, and the presence of unipolar induction within Ceres. Table 1 summarizes the relevant parameters for all 10 cases, which are divided into four categories: Run A, which simulates a single-layer, highly resistive Ceres with no unipolar induction as a "control" case for comparison; Runs B1−B5, which simulate one- and two-layer conductivity structures for Ceres under varying solar wind/IMF conditions and internal conductivity profiles; Runs C1−3, which simulate three-layer conductivity structures with the inclusion of an ocean for Ceres under varying solar wind/IMF conditions and internal conductivities; and Run D, which simulates a moderately conductive, single-layer Ceres with unipolar induction under standard solar wind/IMF conditions. In addition to Table 1, Figure 1 shows the internal conductivity structure models used in each set of runs as described below.

The control case, Run A, used the baseline solar wind and IMF conditions (Collinson et al. 2022), along with a uniform and highly resistive interior conductivity of $\sigma = 10^{-7}$ S m^{-1}. This conductivity is sufficiently low to prevent the formation of any significant internal currents and associated field-line draping at Ceres, similar to that seen in previous simulations of the lunar–solar wind plasma interaction (e.g., Holmström et al. 2012; Vernisse et al. 2013; Poppe 2019; Rasca et al. 2021). These lunar investigations with the Amitis hybrid model are in general agreement with previous plasma and magnetic field observations in near-lunar space (e.g., Halekas et al. 2005; Poppe et al. 2014; Zhang et al. 2014, 2016). Thus, the primary purpose of Run A is to define the solar wind interaction at Ceres considering only solar wind absorption and the formation of a downstream wake and associated currents (e.g., Fatemi et al. 2013; Vernisse et al. 2013). Differences between Run A and later runs can then be clearly attributed to the effects of varying the internal conductivity and/or the presence of unipolar currents at Ceres.

Table 1
List of Model Parameters for All Hybrid Simulations of Ceres

Name	n (cm^{-3})	v (km s^{-1})	$\boldsymbol{B}$ (nT)	σ_m (S m^{-1})	σ_o (S m^{-1})	σ_c (S m^{-1})	Comments
Run A	0.75	400	[−0.5, 1.9, 0.0]	⋯	⋯	10^{-7}	Inert obstacle
Run B1	0.75	400	[−0.5, 1.9, 0.0]	⋯	⋯	10^{-4}	Single layer
Run B2	0.75	400	[−0.5, 1.9, 0.0]	10^{-3}	⋯	10^{-4}	Two layer
Run B3	0.75	400	[−0.5, 1.9, 0.0]	10^{-2}	⋯	10^{-4}	Two layer
Run B4	0.75	400	[0.0, 3.8, 0.0]	10^{-2}	⋯	10^{-4}	Two layer, perp. IMF
Run B5	3.60	700	[0.0, 6.0, 0.0]	10^{-2}	⋯	10^{-4}	Two layer, space weather
Run C1	0.75	400	[−0.5, 1.9, 0.0]	10^{-2}	10^{-1}	10^{-4}	Three layer
Run C2	0.75	400	[−0.5, 1.9, 0.0]	10^{-2}	10^{0}	10^{-4}	Three layer
Run C3	0.75	400	[0.0, 3.8, 0.0]	10^{-2}	10^{0}	10^{-4}	Three layer, perp. IMF
Run D	0.75	400	[−0.5, 1.9, 0.0]	⋯	⋯	10^{-4}	Single layer, with unipolar

Note. n is the solar wind density, v is the solar wind velocity, B is the interplanetary magnetic field, σ_m is the mantle conductivity, σ_o is the ocean conductivity, and σ_c is the crustal conductivity.

Runs B1−B5 explore and quantify the role that differing interior conductivity profiles and upstream conditions have on the solar wind interaction with Ceres. Run B1 simulates a single-layer, moderate-conductivity ($\sigma = 10^{-4}$ S m^{-1}) Ceres with standard solar wind conditions, while Runs B2 and B3 simulate a two-layer (mantle + crust) conductivity structure for Ceres, also with standard solar wind conditions. The two-layer interior conductivity structure of Ceres is taken from the "Dry" model of Grimm et al. (2021), which possesses a ∼35 km thick crust and a 440 km thick mantle. We modified this profile slightly to make the crust 40 km thick and the mantle correspondingly 435 km in order to ensure that the crust was resolved by at least two hybrid grid cells of dimension 20 km. We would naturally aim to resolve the crustal layer with higher resolution (e.g., 10 km grid cells); however, hybrid simulations are naturally limited in resolution by the electron inertial scales, which are ∼5−10 km at Ceres. Nevertheless, based on previous simulations (e.g., Haviland et al. 2019), 20 km resolution is sufficient. In all B runs, the crustal conductivity is held constant at $\sigma_c = 10^{-4}$ S m^{-1} while the mantle conductivity is either $\sigma_m = 10^{-3}$ S m^{-1} (Run B2) or $\sigma_m = 10^{-2}$ S m^{-1} (Runs B3−5). Thus, Runs B1−3 test the effects of increasing mantle conductivity on the overall solar wind interaction with Ceres. In Runs B4 and B5, the two-layer conductivity model for Ceres with conductivities, $[\sigma_m, \sigma_c] = [10^{-2}, 10^{-4}]$, is tested under varying solar wind conditions. Specifically, Run B4 sets the IMF to be fully perpendicular and double in magnitude to test the effects of increased magnetic flux to Ceres. Run B5 models "extreme" solar wind conditions, approximately representative of a coronal mass ejection propagating through the heliosphere. We estimate the parameters for this case by increasing the solar wind density, solar wind velocity, IMF strength, and ion and electron temperatures to values two standard deviations greater than the mean "space weather" conditions listed in Table 1 of Collinson et al. (2022). These extreme conditions yield a solar wind pressure of ∼2.9 nPa, nearly 15× higher than typical conditions at Ceres.

Runs C1−3 test the effects of a three-layer model for Ceres by including a highly conductive ocean layer in between the mantle and crust, adapted from the "Ocean" model in Grimm et al. (2021). We set the mantle, ocean, and crust of Ceres as layers 375, 60, and 40 km thick, respectively, with the only difference between this model and that of Grimm et al. (2021) being again the 40 km thick crust in the hybrid model as opposed to 35 km (see also Figure 1). Runs C1−3 all maintain mantle and crustal conductivities of $\sigma_m = 10^{-2}$ and $\sigma_m = 10^{-4}$ S m^{-1}, respectively, but vary the oceanic conductivity from $\sigma_o = 10^{-1}$ S m^{-1} in Run C1 to $\sigma_o = 10^{0}$ S m^{-1} in Runs C2 and C3, although we note that higher oceanic conductivities ($>10^{1}$ S m^{-1}) are possible with higher relative salt concentrations (e.g., Hand & Chyba 2007). Both Runs C1 and C2 use the standard upstream solar wind parameters. Finally, Run C3 maintains the same internal structure and conductivities as Run C2 but changes the upstream IMF to be both fully perpendicular and double in magnitude, in order to test the effects of increased magnetic field (see also Run B4 for comparison).

Finally, Run D tests the inclusion of unipolar currents through the interior of Ceres on the overall solar wind interaction. Due to the limitations on the magnetic field convection speed through the interior of Ceres, as discussed above in Section 2.2, we limit our investigation of unipolar currents to only one run: a single-layer model for Ceres with conductivity $\sigma_m = 10^{-4}$ S m^{-1} under nominal solar wind conditions. In turn, the results for Run D can be directly compared with Run B1, which has identical internal structure and upstream solar wind conditions only without the inclusion of unipolar currents.

3. Model Results

3.1. Case A: Fully Resistive Ceres

Figure 2 shows the hybrid model results for Run A, including the solar wind density, solar wind velocity, and magnitude of the IMF in the x–y (i.e., equatorial) and x–z (i.e., noon–midnight meridional) planes, respectively, each normalized to their respective upstream values. The formation of a downstream wake is clearly evident in the solar wind density and velocity in both planes due to particle absorption on the dayside of Ceres, extending to greater than 6 R_C downstream. Similar to plasma wakes at other airless, nonconductive bodies, the solar wind refills the plasma void as the solar wind continues to convect downstream (Halekas et al. 2014; Zhang et al. 2014). The magnetic field magnitude downstream of Ceres also shows typical signatures of solar wind interaction with an airless, highly resistive body (e.g., Holmström et al. 2012; Zhang et al. 2014).

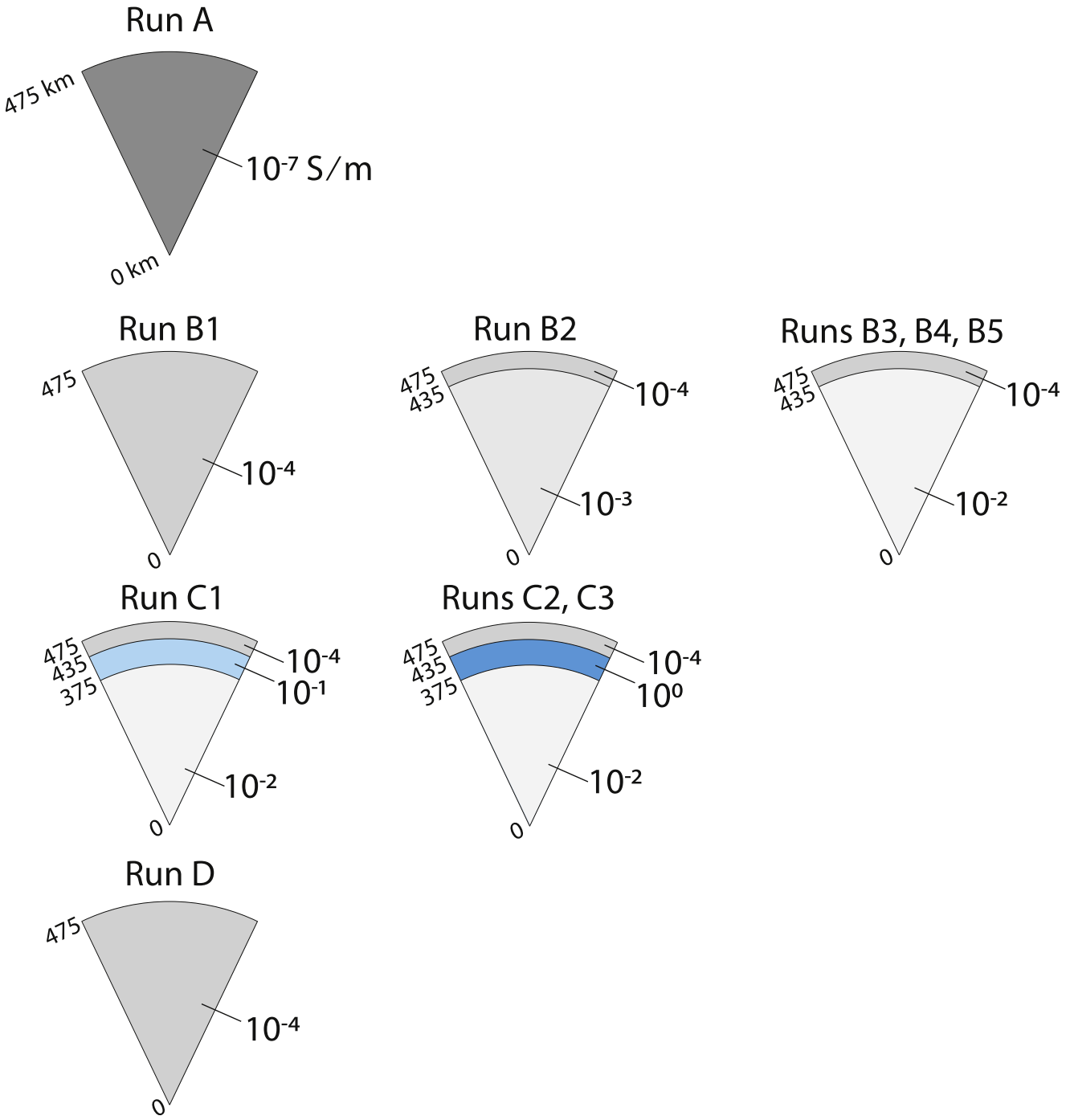

Figure 1. A graphical depiction of the various internal conductivity structures modeled for each set of runs. Runs A and B1 are single-layer models for Ceres with low and moderate internal conductivity, respectfully. Runs B2−B5 explore two-layer models (crust + mantle), while Runs C1−C3 explore three-layer (crust + ocean + mantle) models. Run D explores a single-layer model with contributions from unipolar currents. Radial distances are in units of kilometers and conductivities are in units of siemens per meter.

In the *x*–*y* plane (Figure 2(c)), the IMF is enhanced due to the presence of diamagnetic and/or other plasma currents around the wake boundaries (e.g., see Fatemi et al. 2013; Vernisse et al. 2013; Holmström & Fatemi 2018). In the *x*–*z* plane (Figure 2(f)), both compressional and rarefactional regions are seen in the IMF magnitude, also consistent with previous studies at other airless, highly resistive bodies (e.g., Holmström et al. 2012; Fatemi et al. 2013; Vernisse et al. 2013; Zhang et al. 2014). Thus, Run A represents a standard, baseline model for the interaction of an inert, unmagnetized, and fully resistive body with the solar wind. In particular, the IMF convects through the interior of Ceres with no distortion, and no evidence of upstream perturbations, compressions, or shocks are seen.

3.2. Case B: Two-layer Conductive Ceres

Figure 3 presents a comparison of Run A and Runs B1−3 in the *x*–*y* plane. In addition to the absorption of solar wind plasma at the upstream hemisphere of Ceres and formation of a downstream plasma wake, the densities in Runs B1−3 show

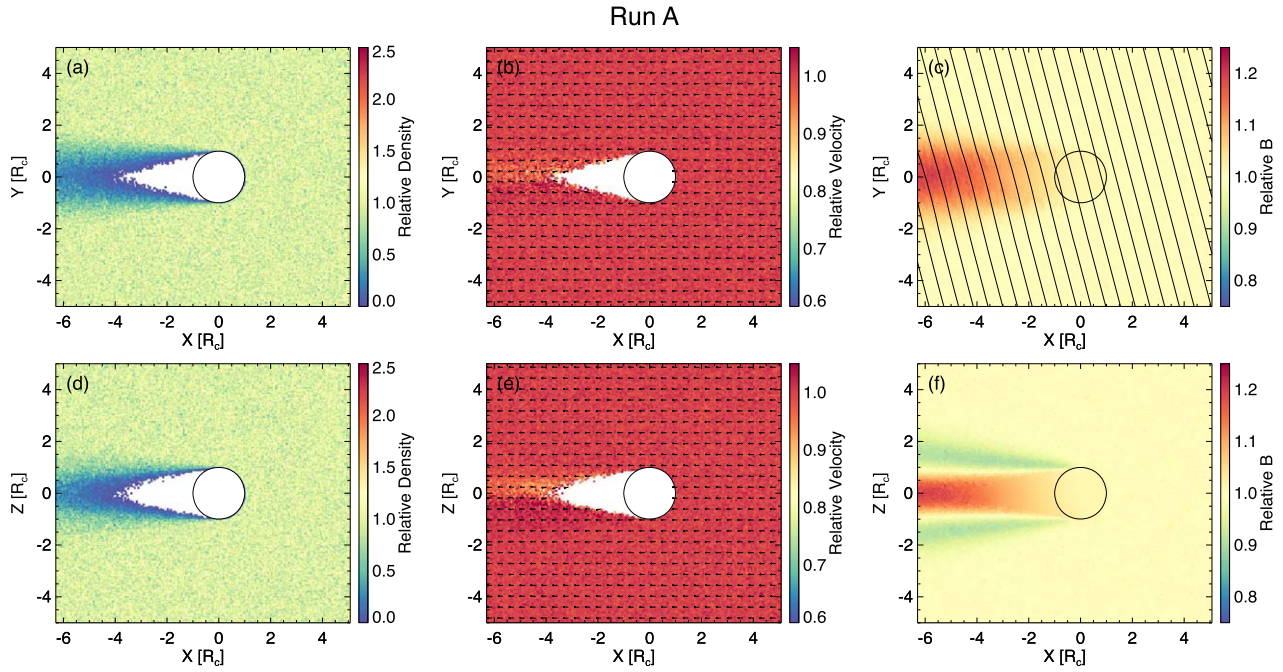

Figure 2. Hybrid model results for Run A in the (a)–(c) *x*–*y* and (d)–(f) *x*–*z* planes, including the solar wind density, solar wind velocity, and magnitude of the interplanetary magnetic field, each normalized to their respective upstream value. Spatial axes are normalized to units of Ceres radii, R_C = 735 km. These results model a completely inert and resistive object in the solar wind as a baseline for comparison.

the presence of compressional wings originating from both flanks of Ceres (Figures 3(b)–(d)). As noted previously, such features are not present in the fully resistive model of Ceres presented in Run A (Figure 3(a)), and thus can be attributed to the presence of conducting layers within Ceres. The distribution of plasma speeds about Ceres in Runs B1−3 (Figures 3(f)–(h)), show perturbations to the solar wind flow different from that seen in Run A (Figure 3(e)). Deceleration in the plasma speed by up to 20% from the upstream solar wind speed is present from the flanks of Ceres along the downstream plasma wake, spatially coincident with the compressional features seen in the densities. Despite the increasing mantle conductivity from Run B1 ($\sigma_m = 10^{-4}$ S m^{-1}) to Run B2 ($\sigma_m = 10^{-3}$ S m^{-1}) to Run B3 ($\sigma_m = 10^{-2}$ S m^{-1}), no appreciable differences are seen across Runs B1−3 in the density or velocity perturbations. In contrast, the magnetic field is increasingly draped over the mantle of Ceres as the interior mantle conductivity rises from Run A through Run B3 (Figures 3(i)–(l)). In Run B1, the magnetic field is draped over much of the dayside hemisphere of Ceres and compressed up to 4.2 times the upstream IMF strength. In Run B2, the magnetic field is increasingly compressed to a subsurface layer on the dayside hemisphere of Ceres as the increased conductivity begins to prevent diffusion through the mantle. Here, the maximum magnetic field is compressed up to 4.75 times the upstream IMF strength. Finally, in Run B3, the IMF is completely excluded from the mantle and entirely compressed within the crust, with maximum compression of approximately 5 times the upstream IMF strength. Additionally, in all of Runs B1−3 a minimum in the magnetic field strength appears on the downstream hemisphere of Ceres, as field lines complete their diffusion through Ceres' interior and are reaccelerated up to the solar wind speed. These magnetic depressions in the low-altitude wake of Ceres are opposite to the magnetic enhancements typically seen within the wakes of resistive airless bodies such as the Moon (e.g., Holmström et al. 2012; Poppe et al. 2014; Zhang et al. 2014) or in the results for Run A here, where Ceres is modeled as highly resistive. Notably, the perturbations in the density, velocity, and magnetic field strength in all of Runs B1−3 are nearly identical *outside* the body, implying the external observations (from, for example, an orbiter) cannot immediately distinguish between a moderate-conductivity mantle (i.e., Run B1, $\sigma_m = 10^{-4}$ S m^{-1}) and a relatively high-conductivity mantle (i.e., Run B3, $\sigma_m = 10^{-2}$ S m^{-1}), at least without resorting to electromagnetic sounding (e.g., Grimm et al. 2021) or other geophysical techniques (e.g., Ermakov et al. 2017; Fu et al. 2017; King et al. 2018).

Having explored the effect of increasing mantle conductivity on the solar wind interaction with Ceres in a two-layer scenario, we now present results exploring variability in the interaction as a function of upstream conditions. Figure 4 shows a comparison of hybrid modeling results from Runs B3, B4, and B5, again with the density, velocity, and magnetic field strength normalized to their respective upstream values (note that the relative magnetic field is plotted logarithmically here to aid comparison over a larger dynamic range). As presented above in Figure 3, the results for Run B3, shown again in the top row of Figure 4, show density compressions, velocity deceleration and deflection, and magnetic field enhancements along the flanks of Ceres and its wake due to the pile-up of IMF lines over the conductive obstacle of Ceres' interior. In comparison, Run B4 is simulated with a stronger and fully perpendicular IMF, thereby increasing the incident magnetic flux to Ceres by a factor of 2. As seen in the middle row of Figure 4, this increased magnetic flux induces greater magnetic pile-up, which in turn produces more intense compressions in the density and greater decelerations in the relative velocity along Ceres' flank. In particular, the maximum density enhancement is a factor of 3 over the upstream solar wind density, and the velocity drops by up to 40% relative to the upstream solar wind velocity. Meanwhile, the normalized magnetic field strengths are generally similar between Runs B3

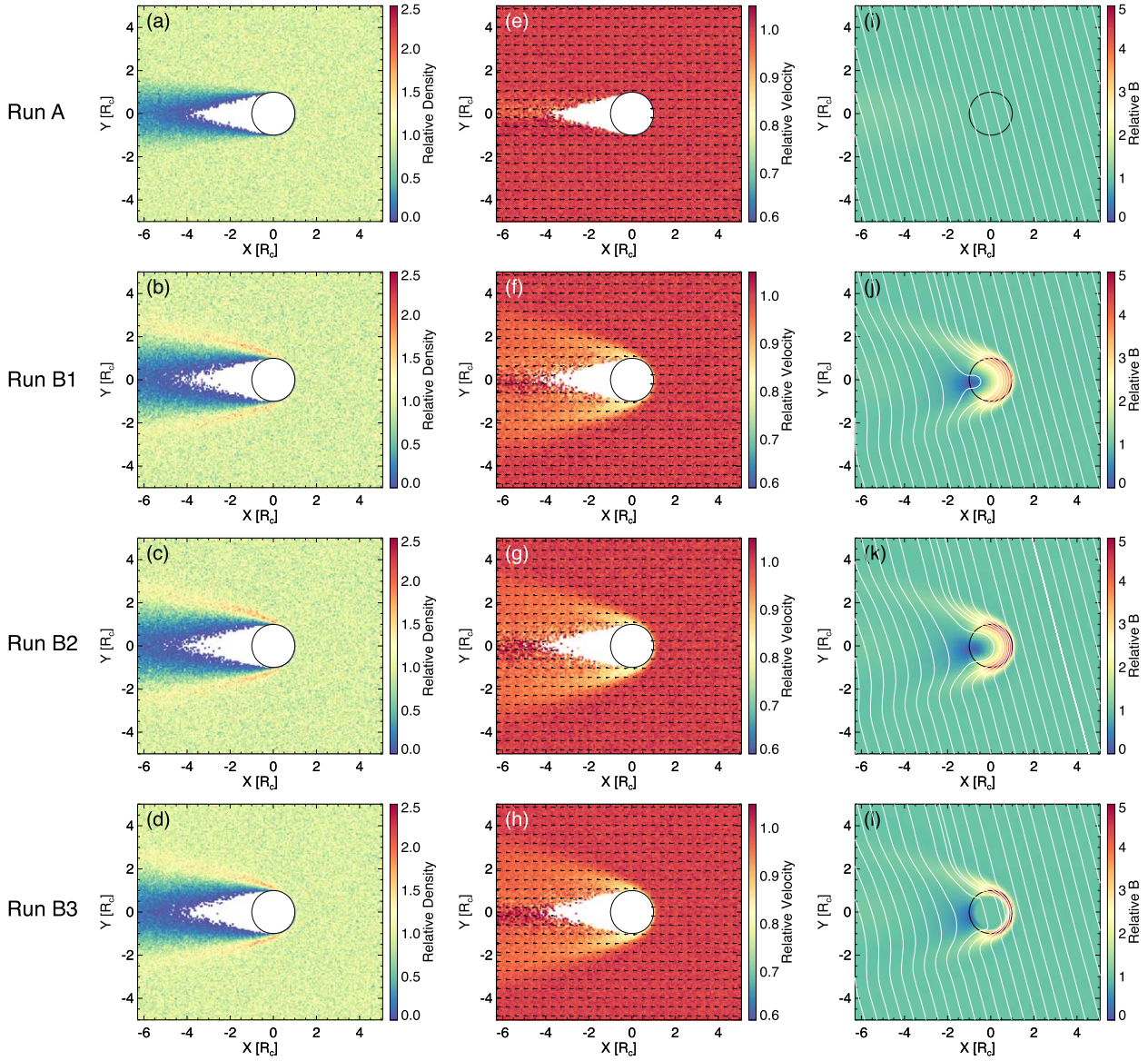

Figure 3. Hybrid model results for Runs A and Runs B1−3 in the *x*–*y* plane, including the solar wind density, solar wind velocity, and magnitude of the interplanetary magnetic field, each normalized to their respective upstream value. These results demonstrate that the inclusion of moderate conductivities within the mantle of Ceres are capable of producing plasma and magnetic field perturbations outside of Ceres.

and B4, although with slightly less subsurface compression and a slightly larger flaring angle in Run B4 (∼34° from the $-\hat{x}$-axis versus ∼25° in Run B3). Finally, Run B5, in the lower row of Figure 4, shows the effect of an extreme space weather event on the solar wind interaction with Ceres. Under these conditions relative to Run B3, the upstream solar wind density, solar wind velocity, and IMF magnitude are increased by factors of ∼5, 1.75, and 3, respectively. The solar wind pressure also increases by over an order of magnitude ($P_{\rm sw}$ = 2.95 nPa) compared to all other runs ($P_{\rm sw}$ = 0.2 nPa). As seen in Figure 4, the interaction of Ceres during an extreme space weather event more closely resembles the results for Run B3 under nominal solar wind conditions. The magnitude of the density compressions and velocity deceleration along the flanks of Ceres are less than that seen in Run B4, for example, despite the increased magnetic flux to Ceres. This can be attributed to the increased solar wind pressure concurrent with the extreme space weather event, which compresses the draped IMFs below the surface of Ceres to a greater degree than Runs B3 or B4. In turn, fields compressed below Ceres' surface do not contribute to the compression and deflection of the solar wind along Ceres' flanks, thereby yielding less significant perturbations to the solar wind plasma as it interacts with Ceres.

3.3. Case C: Three-layer Conductive Ceres

Figure 5 presents the results for Runs C1−3, including the solar wind density, solar wind velocity, and magnetic field magnitude normalized to the respective upstream value in each case. These three cases explore the effects that a third, high-conductivity, oceanic layer in between Ceres' mantle and crust have on the overall solar wind interaction. Runs C1 and C2 include a 40 km thick oceanic layer with conductivities of $\sigma_o = 10^{-1}$ and $\sigma_o = 10^{0}$ S m^{-1}, respectively (see also Figure 1), with nominal upstream solar wind parameters. Similar to Run B3 (in which Ceres possessed only a two-layer mantle/crust structure), perturbations to the solar wind density, solar wind velocity, and magnetic field are seen originating from the flanks

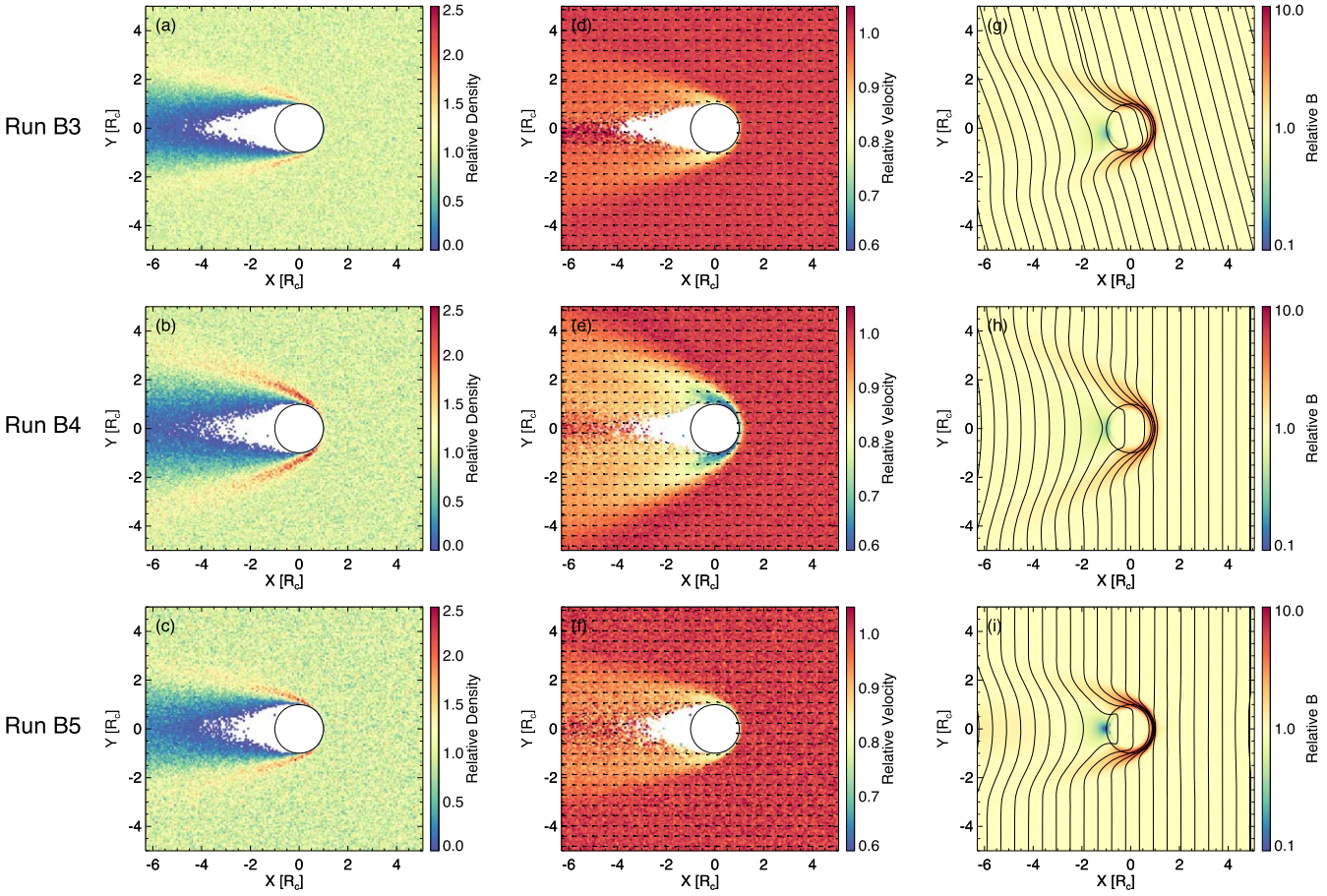

Figure 4. Hybrid model results for Runs B3−5 in the *x*–*y* plane, including the solar wind density, solar wind velocity, and magnitude of the interplanetary magnetic field, each normalized to their respective upstream value. Note that the relative magnetic field is displayed logarithmically to aid in comparison. These results demonstrate that changes in the upstream plasma conditions can yield variations in Ceres' interaction with the solar wind, even for constant-interior-conductivity models.

of Ceres. Finally, Run C3 demonstrates the effect of a fully perpendicular and increased magnitude IMF interacting with a three-layer oceanic structure for Ceres. Similar to Run B4, which also had increased IMF flux to Ceres, the density and velocity perturbations along the flanks of Ceres' wake are greater than those in either of Runs C1 or C2, which are both subjected to nominal solar wind conditions. Indeed, from a simple visual inspection, no appreciable differences in the magnetic fields and/or plasma parameters (density and velocity) are seen between Runs C1/C2 and Run B3 or Run C3 and B4, indicating that the additional inclusion of a high-conductivity oceanic layer above the mantle of Ceres does not appreciably alter the overall solar wind interaction, at least in a steady-state, time-independent sense. In comparison, theoretical investigation of the time-*dependent* response of an oceanic layer within Ceres via electromagnetic sounding techniques does predict an ability to discern the presence of a high-conductivity oceanic layer laying atop a somewhat less conductive mantle (Grimm et al. 2021).

3.4. Case D: Ceres with Unipolar Induction

Figure 6 shows results for Run D, which models the solar wind interaction with Ceres with the inclusion of unipolar-generated currents and magnetic fields. Figure 6 includes (a) the density, (b) the velocity, (c) the IMF and plasma component of the magnetic field, (d) the unipolar component of the magnetic field, and (e) the total magnetic field. As discussed in Section 2.2, the generation of unipolar currents within a body is severely limited by the low diffusion speed of IMF lines through the conductive interior of the body itself. Thus, Run D reverts to a single-layer, moderate-conductivity ($\sigma_m = 10^{-4}$ S m^{-1}) model for the interior structure of Ceres. Here, the IMF and plasma interaction fields (Figure 6(c)), show the standard field-line draping behavior, very similar to that shown for Run B1, which has identical internal structure and solar wind conditions as Run D, only without the unipolar contribution. The unipolar magnetic field, shown in Figure 6(d), demonstrates the expected toroidal behavior, as the unipolar current is out of the page in the planar cut shown here. Notably, the strength of the unipolar magnetic field in this case is only 1.1 nT, far less in magnitude than the IMF and draping fields shown in Figure 6(c). The total magnetic field (Figure 6(e)), indeed shows only minor differences with the IMF and draping fields (Figure 6(c)), demonstrating that even with unipolar currents the solar wind interaction with Ceres is dominated by draping of the IMF and associated plasma perturbations.

To further understand the limitations placed on the unipolar current generation by slow field-line diffusion through the solid body of Ceres and associated field-line draping, we can compare the strength of the unipolar magnetic field obtained in the hybrid model (Figure 6(d)), to the theoretically expected value for unipolar magnetic fields in the absence of a limiting field-line diffusion speed. Using Equation (1), we first calculate

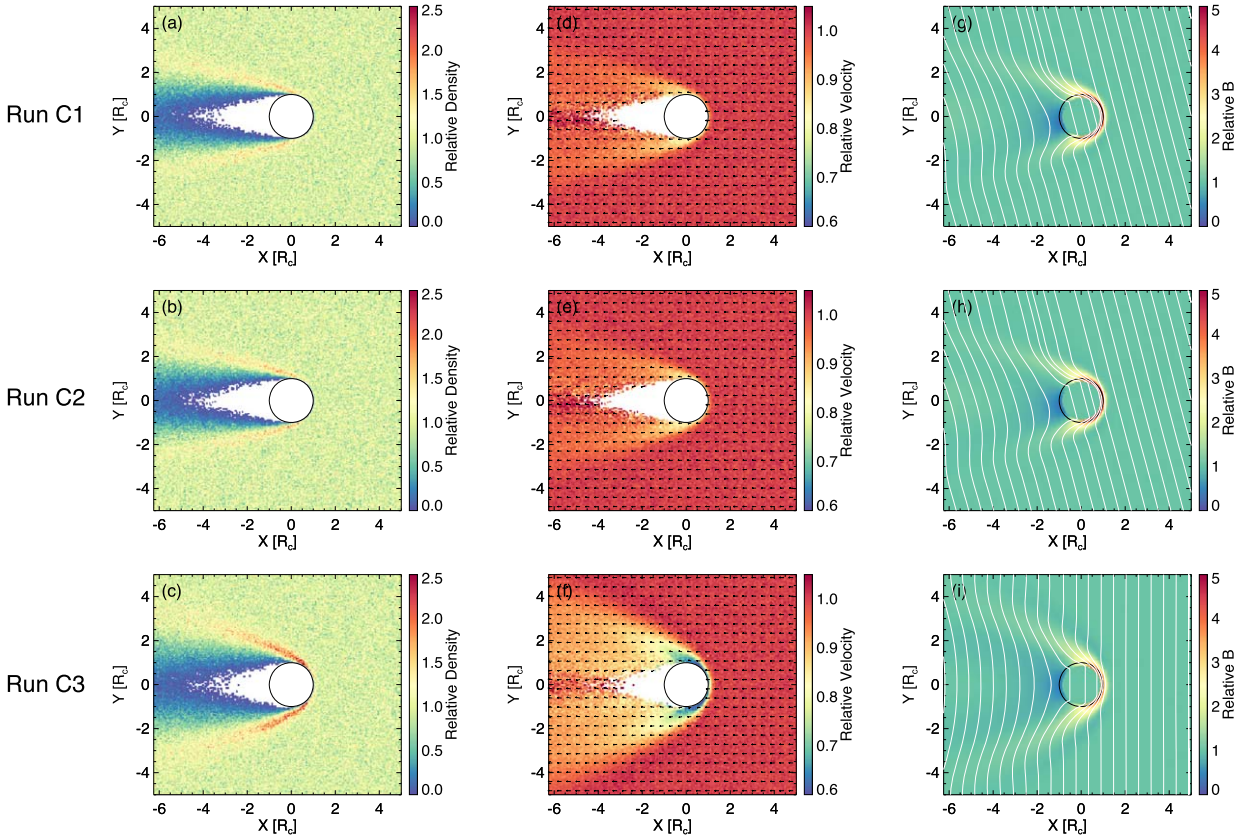

Figure 5. Hybrid model results for Runs C1−3 in the *x*–*y* plane, including the (left) solar wind density, (center) solar wind velocity, and (right) magnitude of the interplanetary magnetic field, each normalized to their respective upstream value. As discussed further in the text, these results demonstrate from a time-independent perspective that inclusion of an ocean as a third layer does not significantly change the overall interaction of Ceres with the solar wind, as compared to the two-layer model results shown in Figures 3 and 4.

the expected unipolar current given the modeled conductivity of Ceres, $\sigma_m = 10^{-4}$ S m^{-1}, the upstream solar wind velocity, $\boldsymbol{v}_{\rm sw} = [400, 0, 0]$ km s^{-1}, and the IMF, $\boldsymbol{B}_{\rm sw} = [0.5, 1.9, 0.0]$ nT. Note that for this estimation we assume the solar wind velocity reaches Ceres' surface undisturbed, which may not fully be the case if unipolar-induced fields are sufficient to slow down the solar wind before it encounters Ceres (e.g., Sonett & Colburn 1968). With the unipolar current vector, $\boldsymbol{J}_{\rm uni}$, a simple application of the Biot–Savart law in the plane perpendicular to $\boldsymbol{J}_{\rm uni}$ provides the unipolar magnetic field at the surface of Ceres. Under the conditions listed above, this calculation yields a theoretically predicted upper limit for the unipolar magnetic field at the surface of Ceres of $B = 22.7$ nT. Furthermore, we can apply the effects of the "flux-tube loss factor," k, from Sonett & Colburn (1968; their Equation (26)), which estimates the amount of magnetic flux diverted around the body by the presence of the unipolar magnetic field. To derive the loss factor, k, Sonett & Colburn (1968) equated an expression for the unipolar magnetic field pressure reduced by a factor of $(1 - k)$ to the incident solar wind pressure. At equilibrium, this expression describes the magnetic back-pressure that unipolar fields impart on the solar wind, thereby causing field lines to convect around the body and not contribute to the unipolar magnetic field formation. Note that the k-factor as derived by Sonett & Colburn (1968) describes *only* the diversion of IMF field lines around the body by induced unipolar fields *before* such field lines actually penetrate through the body (see their Figure 7), and does not reflect any limits from finite field-line diffusion speeds through the body interior. Nevertheless, for the conditions of Run D, we find that $k = 0.355$, and thus Sonett & Colburn (1968) would predict a theoretical unipolar magnetic field of $B = 22.7 \cdot (1.0 - k) = 14.6$ nT. In comparison, the unipolar magnetic field strength obtained from the hybrid simulation, which includes both field-line diversion around the body and restrictions on the field-line diffusion speed through Ceres, is $B_{\rm uni} = 1.1$ nT. This value is far lower than the theoretical value of 14.6 nT and speaks strongly to the limiting effect that restricted field-line diffusion through the conductive interior of Ceres has on the formation of unipolar currents and fields.

4. Discussion and Conclusion

As described above, we have presented hybrid modeling results for a wide range of scenarios characterizing the possible solar wind interactions with asteroid (1) Ceres. At the lower end of the simulated internal conductivities, Run A demonstrates a relatively simple, lunar-like interaction with the solar wind if Ceres' internal structure is highly resistive ($\sigma = 10^{-7}$ S m^{-1}). Standard features of airless body interactions with the solar wind are present, including no upstream perturbations of the solar wind flow, absorption of the solar wind particles on the dayside hemisphere with the concurrent formation of a plasma void (or wake) downstream of the object, and distortions to the IMF downstream of the object due to various plasma currents present generally outside the solid body (e.g., Fatemi et al. 2013). Overall, we do not consider Run A to be a likely scenario for Ceres' interaction with the solar wind, given

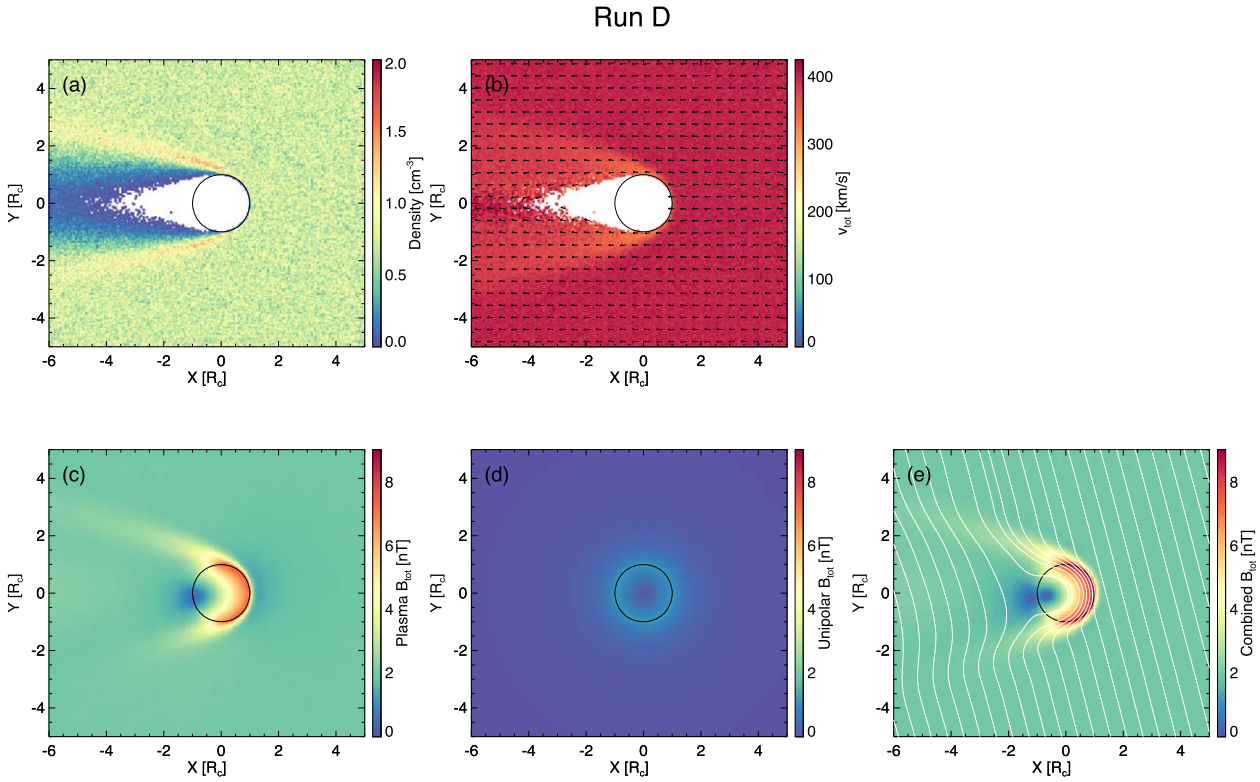

Figure 6. Hybrid model results for Run D in the *x*–*y* plane, including the (a) solar wind density, (b) solar wind velocity, (c) magnitude of the interplanetary magnetic field with plasma interactions with Ceres, (d) magnitude of the unipolar magnetic field, and (e) magnitude of the *total* magnetic field. As discussed further in the text, these results demonstrate that the inclusion of unipolar currents within Ceres have only a very minor effect on the overall interaction of Ceres with the solar wind.

both the observational evidence (e.g., Ermakov et al. 2017; De Sanctis et al. 2020; Bramble & Hand 2022) and associated modeling (e.g., Castillo-Rogez 2011; Neumann et al. 2015; King et al. 2018; Castillo-Rogez et al. 2019; Grimm et al. 2021) suggesting a much more conductive interior for Ceres.

In the context of a moderately to highly conductive interior, Runs B1−5 and Runs C1−3 characterize a range of scenarios for Ceres' solar wind interaction. The common finding through these sets of runs is the field-line draping of the IMF over the conductive interior layers of Ceres, and the subsequent impacts of this field-line draping on the particle behavior outside of Ceres. Understanding this interaction is critical in planning for and interpreting future plasma and magnetic field observations at Ceres. Even in our simplest conductive model, Run B1, which assumed a single-layer, moderate-conductivity ($\sigma = 10^{-4}$ S m^{-1}) interior, field-line draping generates several observable perturbations to Ceres' solar wind interaction. Generally organized along the flanks of Ceres and its wake, these perturbations include enhancements in the magnetic field magnitude and density, and deceleration in the solar wind speed. In a global sense, all three features are readily distinguishable from the relatively inert interaction shown in Run A.

Variations on these general results are seen when comparing Run B1 to Runs B2−5 and Runs C1−3. As the internal mantle conductivity increases over Runs B1, B2, and B3, the interplanetary field-line draping is compressed to progressively thinner layers within the interior of Ceres; however, no significant changes in the particle perturbations outside Ceres' interior are seen. Greater variation in the solar wind interaction with Ceres is seen with changing upstream solar wind and/or IMF conditions, as explored in Runs B4 and B5. As seen in Run B4, enhanced IMF magnitudes yield greater effects in the particle moments; for example, the solar wind speed is reduced by ∼40% along the flanks of Ceres. In contrast, as explored in Run B5, "extreme" solar wind conditions that possess relatively high solar wind dynamic pressures (due to increases in both the solar wind density and speed) tend to compress the draped IMF below the surface of Ceres to a greater degree, yielding less perturbation to the particle moments outside of Ceres' interior than might otherwise be expected. Thus, the interplay of draped magnetic fields over Ceres' conductive interior and the upstream solar wind pressure appears to control much of Ceres' solar wind interaction to first order.

We can compare the results of our simulations with previous work in the literature. The simulation results of both Jia et al. (2017) and Oran et al. (2018) have shown field-line draping over conductive obstacles in the solar wind whereby the draped magnetic field perturbations extend upwards into the solar wind flow by nearly an object radius. This contrasts with our results here, which typically show that the magnetic field enhancements from field-line draping only appear at ∼0.1 object radii (or less) above the surface. In the MHD scales simulated in Jia et al. (2017) and Oran et al. (2018), the solar wind ions are highly magnetized on the scale of the object (i.e., $r_g < R_{obj}$), and thus the solar wind ions can collectively respond to the induced magnetic fields from the body on relatively small length scales. This allows the magnetic field enhancement to be "felt" upstream of the body before the solar wind has had a chance to convect past the obstacle. In contrast, with the hybrid model runs shown here, the reverse is true ($r_g > R_{obj}$), and thus the solar wind ions are relatively demagnetized on the scale of Ceres and its interaction region. In other words, the solar wind ions do not have time to complete a full gyration and

Table 2
A Comparison of the Theoretically Predicted and Numerically Observed Maximum Magnetic Field Enhancement Due to Field-line Draping over the Conductive Interior of Ceres

Name	M_s	β	$M_s\sqrt{\gamma\beta}$	R_M	$\max(B/B_{sw})$
Run B1	9.1	0.94	11.4	47	4.2
Run B2	9.1	0.94	11.4	440	4.8
Run B3	9.1	0.94	11.4	4400	5.0
Run B4	9.1	0.25	5.9	4400	4.2
Run B5	8.6	1.61	14.1	7700	8.3
Run C1	9.1	0.94	11.4	9800	4.3
Run C2	9.1	0.94	11.4	64000	4.3
Run C3	9.1	0.25	5.9	64000	3.8

Note. M_s is the solar wind sonic Mach number, β is the solar wind plasma beta, $A = M_s\sqrt{\gamma\beta}$ is the maximum enhancement predicted from the balance of solar wind and draped magnetic field pressure (see Anand et al. 2022), R_M is the magnetic Reynolds number, and $\max(B/B_{sw})$ is the maximum field enhancement observed in the hybrid model results. All values are unitless.

effectively respond to the magnetic obstacle of the draped fields before they convect past the induced fields and/or Ceres. By doing so, they provide ram pressure all the way down to the surface of Ceres, thereby constraining the draped magnetic field signatures to be much closer to—if not below—the surface of Ceres.

In another study, Anand et al. (2022) have recently reported a series of numerical simulations of solar wind interactions with asteroidal bodies of various conductivities, and in particular have derived theoretical scaling relations for the maximum magnetic enhancement from field-line draping over a body as a function of the ambient magnetic Reynolds number, R_M (see their Figure 2). They have also validated these theoretical scaling relations with numerical simulations. Their work has shown that the peak magnetic field enhancement at a conductive body increases up to a maximum saturation limit, A_{max}, given by

$$A_{max} = \min\left[M_s\sqrt{\gamma\beta}, R_M\right], \quad (2)$$

where M_s is the solar wind Mach number, β is the solar wind beta parameter (ratio of plasma pressure to magnetic pressure), and $\gamma = 5/3$. Table 2 lists a compilation of the various parameters above, including the theoretically predicted maximum magnetic field enhancement via Equation (2) and the maximum observed magnetic field enhancement. For our modeled runs, the magnetic Reynolds number is always much greater than $M_s\sqrt{\gamma\beta}$, implying that the balance of solar wind pressure versus draped magnetic field pressure is primarily what governs the field enhancements. From our simulation results, the maximum field enhancement varies from a factor of 3.8 (Run C3) to 8.3 (Run B5). In all cases, the maximum field enhancement seen in the hybrid model is less than the maximum theoretical predicted enhancement, in agreement with the results from Anand et al. (2022).

We have also explored the role that unipolar induction may play at Ceres in contributing to the overall solar wind interaction. The first theoretical investigations into unipolar currents and fields at airless bodies predicted that unipolar current generation could be an effective mechanism for planetary bodies both without appreciable atmospheres and with sufficient internal conductivity (e.g., Sonett & Colburn 1967, 1968). In contrast, however, our numerical investigation of the potential unipolar contribution to Ceres' interaction with the solar wind has shown that despite its predicted effects at relatively conducting bodies, unipolar currents and their associated magnetic fields are not likely to be a significant effect, in particular due to the strong limitations imposed on the field-line diffusion speed within the body. Notably, Sonett & Colburn (1968) discussed, though did not include, such a limitation in their main body of calculations (i.e., see their Section 23). Furthermore, while not shown here, we simulated a unipolar current with an internal conductivity of $\sigma = 10^{-5}$ S m^{-1}, such that the magnetic diffusion speed was an order of magnitude higher than in our Run D; however, very little unipolar current is present due to the simultaneous limitations imposed by Equation (1) (i.e., less conductivity in the body simply allows less current to flow). This is consistent with discussions in Sonett & Colburn (1968) with regard to transitioning from a weak to strong unipolar interaction between internal conductivities of 10^{-6} to 10^{-3} S m^{-1}. Looking more broadly, our findings here regarding the inefficiency of unipolar induction at Ceres may also have implications for the proposed role of unipolar currents and internal heating at other bodies throughout the solar system (e.g., Herbert & Sonett 1979; Shimazu & Terasawa 1995); however, such a follow-up investigation is left for future work.

While we have considered Ceres to be a fully inert object with no exosphere in this study, previous observations have shown the presence of a water-vapor exosphere, at least sporadically (e.g., Küppers et al. 2014; Roth et al. 2016; Villarreal et al. 2017; Roth 2018; Rousselot et al. 2019). While a full understanding of Ceres' exosphere is not complete, its presence does appear to be correlated with either perihelion transit when surface ice sublimation would be more effective (Küppers et al. 2014; Rousselot et al. 2019) or with the passage of solar energetic particle events which may efficiently sputter significant amounts of water ice from Ceres' surface (Russell et al. 2017; Villarreal et al. 2017). As demonstrated in both Lindkvist et al. (2017) and Jia et al. (2017), ionization of a water-vapor exosphere at Ceres alters the solar wind interaction by introducing heavy ions into the solar wind. These newly born pickup ions mass-load the solar wind immediately upstream of Ceres, causing both a magnetic pile-up and a deflection in the solar wind velocity. Thus, during times when an exosphere is present, the solar wind interaction at Ceres may represent a combination of exospheric mass loading *and* field-line draping over the conductive interior of Ceres. Further modeling combining the two effects is warranted to better understand the relative degree to which each process would contribute to the overall interaction.

Taken in whole, our simulations suggest that Ceres possesses a distinct interaction with the solar wind due to its relatively high predicted internal conductivity. Both the specific internal conductivity structure and the upstream solar wind conditions are key governing factors in determining the overall morphology of both draped IMF field lines and perturbations to the solar wind density and velocity along the flanks of Ceres and its wake. The magnitude of the predicted perturbations to the solar wind density, solar wind velocity, and IMF in the vicinity of Ceres are all readily distinguishable with modern plasma and magnetic field instrumentation. Thus, future missions to (1) Ceres (e.g., Castillo-Rogez et al. 2022) would strongly benefit

from the inclusion of such instrumentation, which would be vital in understanding not only the global morphology of Ceres' solar wind interaction but would also contribute to studies of Ceres' surface evolution from solar wind and energetic particle irradiation (e.g., Kallio et al. 2008; Villarreal et al. 2017; Nordheim et al. 2022) and enable characterizations of Ceres' tenuous exosphere via measurements of escaping exospheric pickup ions, similar to that done at other bodies with similar exospheres (e.g., Teolis et al. 2010; Tokar et al. 2012; Halekas et al. 2015). Finally, characterization of a current or past oceanic layer within Ceres would also help inform studies of Ceres' prospects for habitability in the context of ocean world studies (e.g., Hand et al. 2020).

A.R.P. gratefully acknowledges support from NASA's Solar System Workings Program, grant No. 80NSSC17K0769. S.F. acknowledges support from the Swedish National Research Council, grant No. 2018-03454, and the Swedish National Space Agency, grant No. 115/18. This research was conducted using computational resources provided by the Swedish National Infrastructure for Computing (SNIC), Projects #2020/6-223 and #2021/5-410 at the High Performance Computing Center North (HPC2N), Umeå University, Sweden, and by the Berzelius resource provided by the Knut and Alice Wallenberg Foundation (KAW) at the National Supercomputer Centre (NSC), Linköping, Sweden. S.F. acknowledges Åke Sandgren and Björn Torkelsson at HPC2N and Johan Raber at NSC for their assistance concerning technical and implementational aspects in making the Amitis code run on the Kebnekaise and Berzelius resources. The authors acknowledge G. Collinson for helpful discussions on solar wind parameters in the asteroid belt and two anonymous reviewers for their constructive comments that improved the manuscript.

ORCID iDs

A. R. Poppe https://orcid.org/0000-0001-8137-8176
S. Fatemi https://orcid.org/0000-0002-9450-6672

References

Anand, A., Carroll-Nellenback, J., Blackman, E. G., & Tarduno, J. A. 2022, MNRAS, 509, 2957
Bertucci, C., Duru, F., Edberg, N., et al. 2011, SSRv, 162, 113
Bramble, M. S., & Hand, K. P. 2022, GeoRL, 49, e96973
Castillo-Rogez, J., Neveu, M., Vinogradoff, V., et al. 2022, PSJ, 3, 64
Castillo-Rogez, J. C. 2011, Icar, 215, 599
Castillo-Rogez, J. C., Hesse, M. A., Formisano, M., et al. 2019, GeoRL, 46, 1963
Coates, A. J., & Jones, G. H. 2009, P&SS, 57, 1157
Colburn, D. S., & Reynolds, R. T. 1986, Calculations of Electric Currents in Europa, NASA Technical Memorandum 88347, NASA, https://ntrs.nasa.gov/citations/19870004782
Collinson, G., Chen, L.-J., Jian, L. K., & Dorelli, J. 2022, ApJ, 927, 202
De Sanctis, M. C., Ammannito, E., Raponi, A., et al. 2020, NatAs, 4, 786
Dyal, P., & Parkin, C. W. 1971, JGR, 76, 5947
Ermakov, A. I., Fu, R. R., Castillo-Rogez, J. C., et al. 2017, JGRE, 122, 2267
Fatemi, S., Holmström, M., Futaana, Y., Barabash, S., & Lue, C. 2013, GeoRL, 40, 17
Fatemi, S., Poirier, N., Holmström, M., et al. 2018, A&A, 614, A132
Fatemi, S., & Poppe, A. R. 2018, GeoRL, 45, 39
Fatemi, S., Poppe, A. R., & Barabash, S. 2020, JGRA, 125, e27706
Fatemi, S., Poppe, A. R., Delory, G. T., & Farrell, W. M. 2017, JPhCS, 837, 012017
Fatemi, S., Poppe, A. R., Vorburger, A., Lindkvist, J., & Hamrin, M. 2022, JGRA, 127, e29863
Fu, R. R., Ermakov, A. I., Marchi, S., et al. 2017, E&PSL, 476, 153
Garrick-Bethell, I., Poppe, A. R., & Fatemi, S. 2019, GeoRL, 46, 5778
Glassmeier, K.-H. 2017, RSPTA, 375, 20160256
Goldreich, P., & Lynden-Bell, D. 1969, ApJ, 156, 59
Grimm, R., Castillo-Rogez, J., Raymond, C., & Poppe, A. R. 2021, Icar, 362, 114424
Grimm, R. E., & Delory, G. T. 2012, AdSpR, 50, 1687
Halekas, J. S., Bale, S. D., Mitchell, D. L., & Lin, R. P. 2005, JGRA, 110, A07222
Halekas, J. S., Benna, M., Mahaffy, P. R., et al. 2015, GeoRL, 42, 5162
Halekas, J. S., Poppe, A. R., & McFadden, J. P. 2014, JGRA, 119, 5133
Hand, K. P., & Chyba, C. F. 2007, Icar, 189, 424
Hand, K. P., Khurana, K. K., & Chyba, C. F. 2011, JGRE, 116, E04010
Hand, K. P., Sotin, C., Hayes, A., & Coustenis, A. 2020, SSRv, 216, 95
Haviland, H., Poppe, A. R., Fatemi, S., Delory, G. T., & de Pater, I. 2019, GeoRL, 46, 4151
Herbert, F. 1989, Icar, 78, 402
Herbert, F., & Lichtenstein, B. R. 1980, Icar, 44, 296
Herbert, F., & Sonett, C. P. 1979, Icar, 40, 484
Holmström, M., & Fatemi, S. 2018, in Electric Currents in Geospace and Beyond, Vol. 235, ed. A. Keiling, O. Marghitu, & M. Wheatland (New York: Wiley)
Holmström, M., Fatemi, S., Futaana, Y., & Nilsson, H. 2012, EP&S, 64, 237
Jia, X., Slavin, J. A., Gombosi, T. I., et al. 2015, JGRA, 120, 4763
Jia, Y.-D., Villarreal, M. N., & Russell, C. T. 2017, JGRA, 122, 4976
Kallio, E., Wurz, P., Killen, R., et al. 2008, P&SS, 56, 1506
Khan, A., Connolly, J. A. D., Olsen, N., & Mosegaard, K. 2006, E&PSL, 248, 579
King, S. D., Castillo-Rogez, J. C., Toplis, M. J., et al. 2018, M&PS, 53, 1999
Küppers, M., O'Rourke, L., Bockelée-Morvan, D., et al. 2014, Natur, 505, 525
Laine, R. O., & Lin, D. N. C. 2012, ApJ, 745, 2
Ledvina, S. A., Ma, Y.-J., & Kallio, E. 2008, SSRv, 139, 143
Li, J., Ferrario, L., & Wickramasinghe, D. 1998, ApJL, 503, L151
Lindkvist, J., Holmström, M., Fatemi, S., Wieser, M., & Barabash, S. 2017, GeoRL, 44, 2070
Luhmann, J. G., Ledvina, S. A., & Russell, C. T. 2004, AdSpR, 33, 1905
Menzel, R. L., & Roberge, W. G. 2013, ApJ, 776, 89
Mittelholz, A., Grayver, A., Khan, A., & Kuvshinov, A. 2021, JGRE, 126, e06980
Neumann, W., Breuer, D., & Spohn, T. 2015, A&A, 584, A117
Nordheim, T. A., Castillo-Rogez, J. C., Villarreal, M. N., Scully, J. E. C., & Costello, E. S. 2022, AsBio, 22, 509
Olhoeft, G. R., Frisillo, A. L., & Strangway, D. W. 1974, JGR, 79, 1599
Oran, R., Weiss, B. P., & Cohen, O. 2018, E&PSL, 492, 222
Park, R. S., Konopliv, A. S., Bills, B. G., et al. 2016, Natur, 537, 515
Park, R. S., Vaughan, A. T., Konopliv, A. S., et al. 2019, Icar, 319, 812
Poppe, A. R. 2019, JGRA, 124, 6927
Poppe, A. R., Fatemi, S., Halekas, J. S., Holmström, M., & Delory, G. T. 2014, GeoRL, 41, 3766
Rasca, A. P., Fatemi, S., Farrell, W. M., Poppe, A. R., & Zheng, Y. 2021, JGRA, 126, e28789
Roth, L. 2018, Icar, 305, 149
Roth, L., Ivchenko, N., Retherford, K. D., et al. 2016, GeoRL, 43, 2465
Rousselot, P., Opitom, C., Jehin, E., et al. 2019, A&A, 628, A22
Russell, C. T., Capaccioni, F., Coradini, A., et al. 2007, EM&P, 101, 65
Russell, C. T., Raymond, C. A., Ammanito, E., et al. 2017, Sci, 353, 1008
Saur, J. 2004, JGRA, 109, A01210
Schwartz, K., Sonett, C. P., & Colburn, D. S. 1969, Moon, 1, 7
Shi, Z., Rong, Z. J., Fatemi, S., et al. 2022, GeoRL, 49, e98415
Shimazu, H., & Terasawa, T. 1995, JGR, 100, 16923
Sonett, C. P., & Colburn, D. S. 1967, Natur, 216, 340
Sonett, C. P., & Colburn, D. S. 1968, PEPI, 1, 326
Sonett, C. P., Colburn, D. S., Schwartz, K., & Keil, K. 1970, Ap&SS, 7, 446
Teolis, B. D., Jones, G. H., Miles, P. F., et al. 2010, Sci, 330, 1813
Tokar, R. L., Johnson, R. E., Thomsen, M. F., et al. 2012, GeoRL, 39, L03105
Vernisse, Y., Kriegel, H., Wiehle, S., Motschmann, U., & Glassmeier, K.-H. 2013, P&SS, 84, 37
Villarreal, M. N., Russell, C. T., Luhmann, J. G., et al. 2017, ApJL, 838, L8
Walters, N., Farihi, J., Marsh, T. R., et al. 2021, MNRAS, 503, 3743
Zhang, H., Khurana, K. K., Kivelson, M. G., et al. 2014, JGRA, 119, 5220
Zhang, H., Khurana, K. K., Kivelson, M. G., et al. 2016, JGRA, 121, 10698